


Microresonator dynamics with frequency-dependent Kerr nonlinearity

Ambareesh Sahoo* and Amarendra K. Sarma

Department of Physics, Indian Institute of Technology Guwahati, Assam 781039, India (Received 13 April 2021; revised 8 July 2021; accepted 2 August 2021; published 18 August 2021)

We investigate the ultrafast nonlinear dynamics in a silica ringresonator composed of a silver-nanoparticle-doped core that exhibits rapidly varying frequency-dependent Kerr nonlinearity that even changes sign across a specific frequency, defined as zero-nonlinearity frequency. We model optical propagation in such a resonator through a modified Lugiato-Lefever equation, revealing that the formation of bright cavity solitons can be possible in both positive and negative nonlinearity domains. The intrapulse Raman scattering along with the frequency-dependent Kerr nonlinearity modify the stability and the dynamics of cavity solitons, which we analyze using a bistability analysis, intracavity modulation-instability analysis, and semianalytical variational approach. Our derived analytical results agree well with the direct numerical solutions of the Lugiato-Lefever equation. The generation of a dispersive wave from a cavity soliton encountering higher-order dispersion is also influenced by the location of the zero-nonlinearity frequency, which we describe by providing a modified phase matching equation. Our results and analysis provide a framework for better understanding the dynamics of cavity solitons and their interactions in two different bright-solitonic domains with possible applications in dual-pump spectroscopy, formation of soliton molecules, and counterpropagating solitons to other fields.

DOI: [10.1103/PhysRevA.104.023513](https://doi.org/10.1103/PhysRevA.104.023513)**I. INTRODUCTION**

Microresonators are versatile photonic platforms that support stable optical pulses that round trip indefinitely, known as optical cavity solitons (CSs) [1]. These CSs are ideal candidates for generating frequency combs with applications ranging from optical frequency measurement, spectroscopy, atomic clocks, and astronomy to other fundamental areas of physics [2,3]. As the CSs are the extension of optical solitons in the nonconservative dissipative systems, they emerge through a double balance mechanism between the group-velocity dispersion (GVD) and Kerr nonlinearity, and between losses and continuous-wave (cw) coherent external pumping [1]. The evolution of CSs and the corresponding frequency comb dynamics is described by the Lugiato-Lefever equation (LLE), a damped-driven nonlinear Schrödinger equation (NLSE) [4], where the CSs arise when the system exhibits subcritical instability [4–6]. Over the years, the research on temporal CSs and microresonator-based frequency combs has been carried out in investigating soliton molecules [7], ultrafast soliton dynamics [8], symmetry breaking of counterpropagating light [9], non-Hermitian optics [10], resonator with quartic dispersion [11], Dirac solitons in microresonators [12], etc. Also, in silica resonators, the influence of the Raman effect on Kerr domain walls and localized structures has recently been investigated, revealing interesting stabilization dynamics and bifurcation structure of the domain walls and localized structures [13–15]. Most of the studies of optical CSs are carried out in either anomalous dispersion (AD) [16,17] or normal dispersion (ND) [18,19] domains

with strict self-focusing (positive) Kerr nonlinearity. However, engineered metamaterials [20–23] show promising avenues to study optical pulse dynamics beyond self-focusing nonlinearity. In this case, self-defocusing (negative) nonlinearity plays the central role, enabling the formation of stable optical pulses and their manipulations in the ND domain [21,24–26]. In earlier works, the consequences of negative nonlinearity have been reported in both spatial and temporal domains, where the formation of stable structures and their dynamics are studied [27–30]. However, most of the studies on microresonator-based frequency combs are limited to the self-focusing nonlinearity.

This paper studies the nonlinear optical pulse dynamics and the corresponding frequency combs in a passive silica microresonator whose core is doped with silver nanoparticles [21,31]. For such a doped fiber, the optical Kerr nonlinear parameter varies rapidly with frequencies (wavelengths) and can have positive as well as negative values across a zero-crossing point of the frequency axis, defined as zero-nonlinearity frequency (ZNF). In such an optical medium, the relative locations of zero-dispersion frequency (ZDF) and ZNF lead to four different optical domains; among them, two are solitonic (dispersion and nonlinearity with opposite signs) and two are nonsolitonic (dispersion and nonlinearity with the same signs). In this work, we study the comb dynamics in two bright-solitonic domains and investigate how this frequency-dependent nonlinearity affects the stability and existence of CSs. We theoretically investigate the stability criteria and complex dynamics of the CS under various perturbations using Lagrange’s variational method [32–36], where we consider an ansatz whose parameters are allowed to evolve over round trips. The underlying physics of complex cavity dynamics of CSs can be revealed through Ritz’s

*ambareeshs@iitg.ac.in

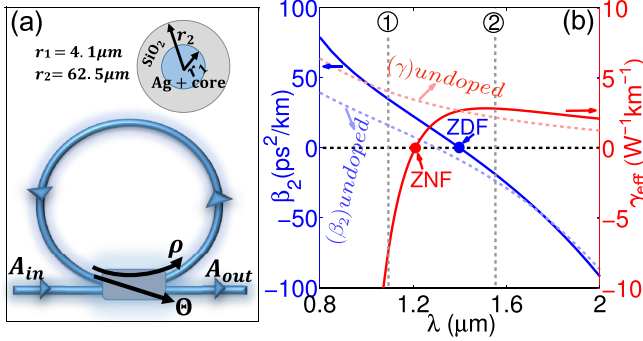


FIG. 1. (a) Schematic diagram of a silica ring resonator with a single bus waveguide with power reflection and transmission coefficients of ρ and Θ . The zoomed cross section of the fiber ring is depicted at the top. (b) The GVD and nonlinearity profiles of the fundamental mode of the doped fiber are shown by the solid blue and red lines, respectively, for a filling fraction of $f = 6 \times 10^{-3}$ [21]. The GVD and nonlinearity profiles of the undoped fiber with the same geometry are also depicted by light dashed lines. The locations of the ZNF and ZDF are denoted by circles. The location of two inputs are indicated by ① (for $\lambda_0 = 1.08 \mu\text{m}$) and ② (for $\lambda_0 = 1.55 \mu\text{m}$).

optimization principle, which leads us to the equation of motion of different pulse parameters. Exploiting the cw bistability analysis [37,38] and intracavity modulation-instability (MI) analysis [39], we further get into the detail of modified stability conditions under perturbations. Also, in a silica resonator, the interplay between ZNF and intrapulse Raman scattering (IRS) leads to the control and manipulation of CS dynamics. We provide a detailed theoretical analysis revealing the properties of CSs in such a frequency-dependent Kerr nonlinear medium, both numerically and analytically, and compare the results. In this context, the interplay between the ZDF and ZNF leads to the manipulation of the dynamics of CS-mediated dispersive waves (DWs). We provide a modified phase matching (PM) equation that accurately predicts the spectral location of the DW in the presence of the ZNF.

II. SETUP

To study the nonlinear pulse dynamics in a fiber resonator with frequency-dependent Kerr nonlinearity (FDKN), we consider a realistic single-mode silica fiber [40] whose core is doped with silver nanoparticles [schematically shown in Fig. 1(a)] [21,25,41]. For such a doped fiber, the frequency-dependent third-order optical Kerr nonlinear parameter [$\gamma_{\text{eff}}(\omega)$] with a zero-crossing frequency (defined as ZNF) is depicted in Fig. 1(b). $\gamma_{\text{eff}}(\omega)$ is calculated from the Maxwell-Garnett theory [42] in the framework of the theory of effective composite medium [43], the specifics of which can be found in Refs. [21,25,31]. Earlier experimental studies have confirmed the existence of frequency-dependent nonlinearity, as well as the presence of ZNF in metal-nanoparticle-doped composite media [44,45]. In addition, the experimentally measured Raman gain spectrum in silver-nanoparticle-doped silica fiber indicates that the doping of nanoparticles does not change the gain spectrum from that of the undoped silica fiber [31], suggesting that nanoparticle doping only affects the Kerr term. On the basis of these experimental findings,

ultrashort optical pulse propagation in such a doped fiber is modeled as follows [25,46]: $i\partial_z A + i(\alpha_l/2)A + \hat{D}(i\partial_t)A + \hat{\mathcal{F}}[\gamma_{\text{eff}}(\omega)](1 - f_R)|A|^2 A + \hat{\mathcal{F}}[\gamma(\omega)]f_R h_R \otimes |A|^2 A = 0$, where $A(z, t)$ is the optical pulse envelope, α_l is the linear loss coefficient, \hat{D} is the dispersion operator, and $\hat{\mathcal{F}}$ denotes the inverse Fourier-transform operator. Also, $\gamma(\omega)$ defines the third-order nonlinear parameter of undoped SiO_2 of the same geometry that contains an additional self-steepening term. Further, h_R represents the usual time-domain description of the Raman response function, with a fractional Raman contribution of f_R [47]. Like the GVD parameter, γ_{eff} also contains all the higher-order terms defined from the Taylor series expansion around a central frequency ω_0 . While γ_{eff} shows a rapid variation with frequency and changes its numeric signs across a ZNF (the analogy is the same as that of the ZDF), $\gamma(= \gamma_{\text{undoped}})$ is strictly positive [schematically depicted in Fig. 1(b)]. For such a doped fiber resonator [Fig. 1(a)] with power reflection and transmission coefficients ρ and Θ , the intracavity round-trip boundary condition [1] $[A^{(m+1)}(0, \tau) = \sqrt{1 - \Theta} A^{(m)}(0, \tau) e^{i\Phi_0} + \sqrt{\Theta} A_{\text{in}}(\tau)]$ along with the modified NLSE [25] describe the evolution equation for CSs, formally known as the mean-field LLE.

In a very recent work [48], a more appropriate description of the NLSE-type model equation has been proposed in the context of FDKN, which describes the similar pulse dynamics as predicted by our adopted model [25] with additional photon number conservation. However, the mathematical form of the proposed equation is not simple in terms of ansatz functions and nonlinearity, and it is not possible to deduce the mean-field LLE. The implication of the variational method is also difficult in this case. For these reasons, we rely on the old model equation for FDKN, as these two models predict the similar pulse propagation behavior in both domains. Moreover, under suitable approximation, these two models give a similar mathematical form under positive nonlinearity [49].

III. MEAN-FIELD MODEL

The passive cavity dynamics in the presence of FDKN in a silica microresonator with intracavity field amplitude $u(t, \tau)$ is mathematically modeled by the dimensionless mean-field LLE [1,4] which includes self-steepening, IRS, higher-order dispersion (HOD), and frequency-dependent nonlinear effects (up to first order) in the long pulse domain as

$$\begin{aligned} \frac{\partial u}{\partial t} = & \left[-(1 + i\Delta) + i \sum_{n \geq 2} \delta_n \left(i \frac{\partial}{\partial \tau} \right)^n \right] u + S \\ & + i \left[a(1 - f_R)|u|^2 u + i\mu_{1\text{eff}}(1 - f_R) \frac{\partial(|u|^2 u)}{\partial \tau} \right. \\ & \left. + \Gamma f_R \left(1 + i\tau_{\text{sh}} \frac{\partial}{\partial \tau} \right) |u|^2 u - \Gamma \tau_{R0} \frac{\partial(|u|^2)}{\partial \tau} \right], \quad (1) \end{aligned}$$

where $a = \text{sgn}(\gamma_{0\text{eff}})$, $\Gamma = \gamma_0/|\gamma_{0\text{eff}}|$. Also, at an operating frequency ω_0 near to the ZNF, $\gamma_{\text{eff}}(\omega) \approx \gamma_{0\text{eff}} + \gamma_{1\text{eff}}(\omega - \omega_0)$ and $\gamma(\omega) \approx \gamma_0 + \gamma_1(\omega - \omega_0)$. Note that $\gamma_{1\text{eff}}$ is the slope of the rapidly varying nonlinearity profile of the nanoparticle-doped composite fiber that gives the location of the ZNF, while γ_1 is the usual self-steepening in the undoped conventional fiber. The calculated values of these parameters and

TABLE I. The rescaling of the parameters of Eq. (1) are adopted from Refs. [38,50]. L , t_R , and $\alpha_t = (\alpha_l L + \Theta)/2$ are the cavity round-trip length, cavity round-trip time, and total cavity loss, respectively. Here, $\Theta = 0.1$ for a 90/10 coupler, and the experimentally measured linear loss of the doped fiber in the working wavelengths is $\alpha_l \approx 2$ dB/m [31]. At $\lambda_0 = 1.08 \mu\text{m}$: $\gamma_{0\text{eff}} = -8.839 \text{ W}^{-1} \text{ km}^{-1}$, $\gamma_{1\text{eff}} = -7.936 \times 10^{-2} \text{ W}^{-1} \text{ km}^{-1} \text{ ps}$, $\gamma_0 = 4.083 \text{ W}^{-1} \text{ km}^{-1}$, $\gamma_1 = 3.713 \times 10^{-3} \text{ W}^{-1} \text{ km}^{-1} \text{ ps}$, $\beta_2 = 36.506 \text{ ps}^2/\text{km}$, and $\beta_3 = 7.307 \times 10^{-2} \text{ ps}^3/\text{km}$. At $\lambda_0 = 1.55 \mu\text{m}$: $\gamma_{0\text{eff}} = 2.915 \text{ W}^{-1} \text{ km}^{-1}$, $\gamma_{1\text{eff}} = -2.280 \times 10^{-4} \text{ W}^{-1} \text{ km}^{-1} \text{ ps}$, $\gamma_0 = 2.156 \text{ W}^{-1} \text{ km}^{-1}$, $\gamma_1 = 3.537 \times 10^{-3} \text{ W}^{-1} \text{ km}^{-1} \text{ ps}$, $\beta_2 = -18.598 \text{ ps}^2/\text{km}$, and $\beta_3 = 1.647 \times 10^{-1} \text{ ps}^3/\text{km}$.

Description	Rescaled/normalized as
Slow time t	$\alpha_t t / t_R \rightarrow t$
Fast time τ	$\tau \sqrt{2\alpha_t / [\beta_2(\omega_0) L]} \rightarrow \tau$
Fast time normalization	
timescale τ_s	$\tau_s = \sqrt{ \beta_2(\omega_0) L / (2\alpha_t)}$
Intracavity field amplitude A	$u = A \sqrt{ \gamma_{0\text{eff}} L / \alpha_t}$
Driving field strength A_{in}	$S = A_{in} \sqrt{ \gamma_{0\text{eff}} L \Theta / \alpha_t^3}$
Phase detuning δ_0	$\Delta = \delta_0 / \alpha_t$
n th-order dispersion parameter $\beta_n(\omega)$	$\delta_n = 2\beta_n(\omega) / [n! \beta_2(\omega_0) \tau_s^{n-2}]$
Slope of the rapidly varying $\gamma_{\text{eff}}(\omega)$, $\gamma_{1\text{eff}}$	$\mu_{1\text{eff}} = \gamma_{1\text{eff}} / [\gamma_{0\text{eff}}(\omega_0) \tau_s]$
IRS parameter T_R	$\tau_R = T_R / \tau_s$
Self-steepening parameter	$\tau_{\text{sh}} = \gamma_1 / [\gamma_0(\omega_0) \tau_s]$

the other rescaled parameters are given in Table I. Here we consider both the bright-solitonic domains ($\beta_2 \times \gamma_{\text{eff}} < 0$) according to the launching conditions $\lambda_0 = 1.08 \mu\text{m}$ (ND with self-defocusing nonlinearity) denoted by ① and $\lambda_0 = 1.55 \mu\text{m}$ (AD with self-focusing nonlinearity) denoted by ②, and study the individual intracavity field dynamics. For that, we first solve the LLE [Eq. (1)] numerically without extra perturbations, i.e., in the absence of HOD ($\delta_n > 2 = 0$), self-steepening ($\tau_{\text{sh}} = 0$), IRS ($\tau_R = 0$), and ZNF ($\mu_{1\text{eff}} = 0$). This brings Eq. (1) to the unperturbed LLE, whose temporally localized and steady-state solution is disclosed by the unperturbed CS. The dotted trace on the top of each panel in Fig. 2 shows unique features of the unperturbed CS. In the time domain, it comprises an ultrashort pulse that sits on top of a nonzero cw background field with remarkable stability and has two side lobes. In the frequency domain, the relatively broadband comb wings indicate the presence of a short pulse. The numerical solution also reveals that the existence of bright CSs in ① is strictly limited by the negative detuning (cold detuning) (i.e., $-\Delta$). In contrast, ② follows the usual conventional case (warm detuning) [38]. The numerical solution of Eq. (1) is obtained by a split-step Fourier method [47] with a fourth-order Runge-Kutta algorithm embedded in it [51]. For our simulation, we consider the characteristic pulse duration of $\tau_s = 100$ fs. In Figs. 2(a) and 2(b), we plot the evolution of a CS in temporal and spectral domains, respectively, for ① under the effect of FDKN with all perturbations present in the system (i.e., $\delta_3 = 0.0067$, $f_R = 0.245$, $\tau_R = 0.03$, $\tau_{\text{sh}} = 0.0091$, and $\mu_{1\text{eff}} = -0.0898$).

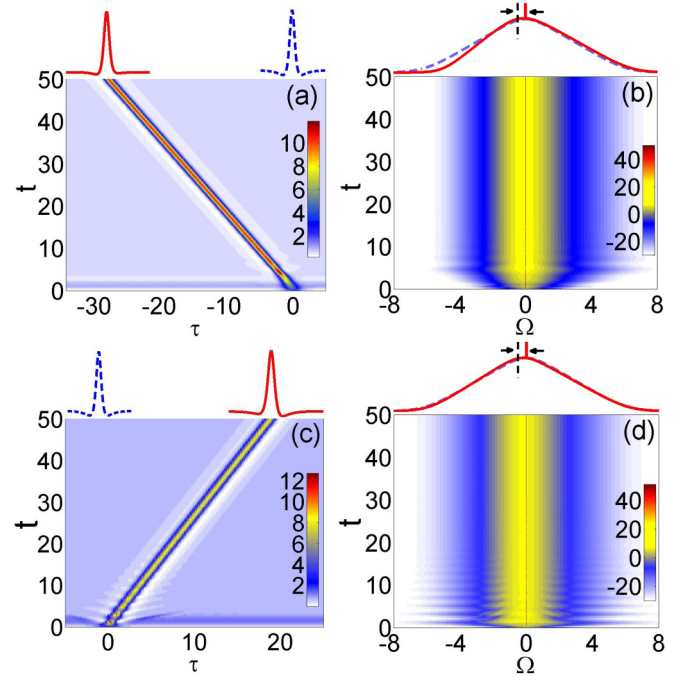


FIG. 2. (a) Temporal (τ) and (b) spectral [$\Omega = (\omega - \omega_0)\tau_s$] evolution of a CS over t for ① with $X = 4.5$, $\Delta = -3$. (c) and (d) describe the same for ② with $X = 4.5$, $\Delta = 3$. The other realistic parameters are defined in the main text. The temporal and spectral profiles of the unperturbed (dotted trace) and perturbed (solid line) CSs at the output are also depicted on the overhead of each panel.

Similarly, in Figs. 2(c) and 2(d), we plot the same for ② with the parameters of $\delta_3 = 0.0295$, $f_R = 0.245$, $\tau_R = 0.03$, $\tau_{\text{sh}} = 0.0164$, and $\mu_{1\text{eff}} = -7.8212 \times 10^{-4}$. In both cases, IRS leads to frequency redshifting. As a result of this frequency shift, the CS accelerates in the ND domain and slows down in the AD domain. The resulting combined role of the ZNF ($\mu_{1\text{eff}}$) and self-steepening (τ_{sh}) also controls the CS dynamics and introduces an asymmetry in the comb spectrum. Note that in both cases, the impact of small δ_3 on the CS is not significant and a signature of DW is not evident in Fig. 2. However, a relatively strong δ_3 perturbs the CS to generate DW across the ZDF. The impact of ZNF on the CS-mediated DW is discussed in Sec. VII. The numerical solution also reveals that the generation of CS is limited by a certain range of controlling parameters (S , Δ) outside of which CS cannot be excited. This range depends on the physical perturbations present in the system. Further, it also reveals that for a fixed set of S and Δ , selective excitation and deexcitation of CSs are possible by changing the location of the ZNF. In the following sections, we try to understand how the CS dynamics are affected by various physical processes using steady-state cw bistability analysis, MI analysis, and variational analysis.

IV. HOMOGENEOUS STEADY-STATE SOLUTIONS AND CW BISTABILITY ANALYSIS

CW bistability analysis in passive Kerr resonators is an analytical tool that helps us to understand the stability of the homogeneous solutions of the intracavity field with respect to the control parameters of the system [1,37]. This analysis is

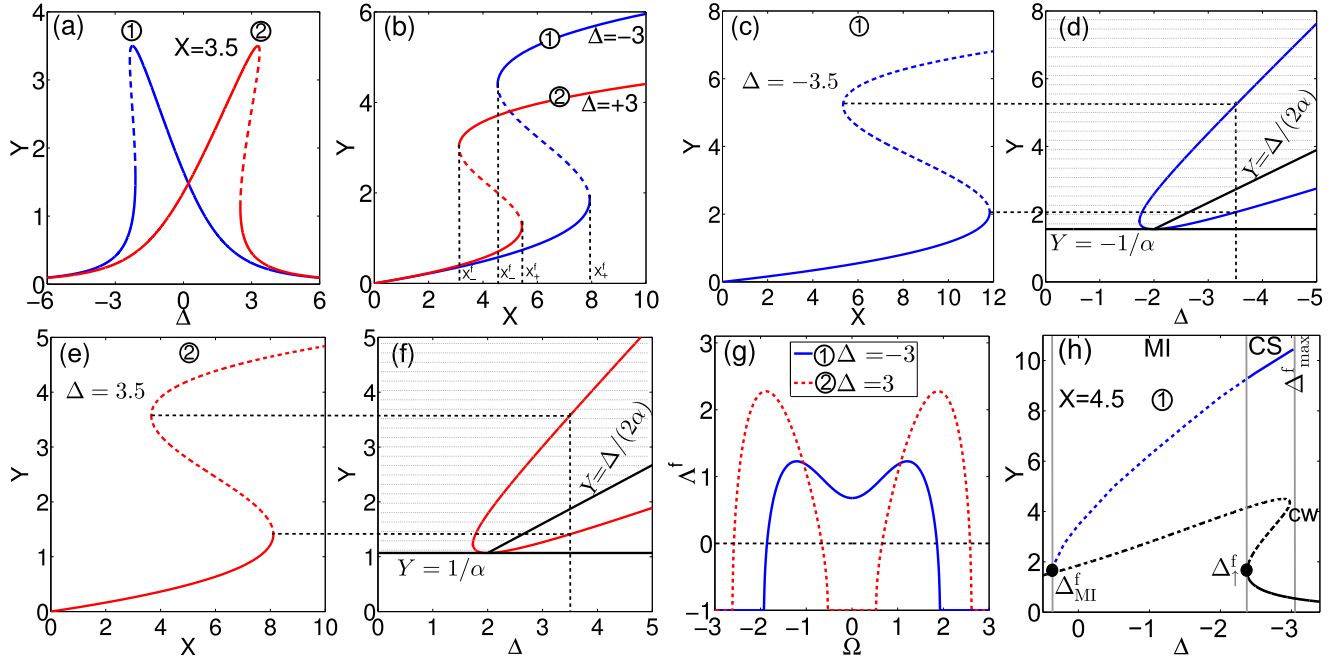


FIG. 3. (a) Kerr bistability curves in (Δ, Y) parameter space from Eq. (5) and (b) cw bistability S curves in (X, Y) from Eq. (2) for two launching conditions. The dashed portions indicate the cw-unstable solutions. The turning points in (b) are indicated by X_{\pm}^f . (c),(e) Kerr bistability curves are mapped with (d),(f) the corresponding intracavity MI regions. The dashed curves in (c) and (e) are MI-unstable solutions, and the shaded areas in (d) and (f) indicate the MI-unstable regions. (g) MI gain spectrum $\Delta^f(\Omega)$ in the presence of FDKN for two launching conditions with $Y = 3.5$. (h) The intracavity cw solutions (black curve), peak intensity of the MI branch (dashed blue curve), and peak intensity of the CSs (solid green curve) as a function of Δ under FDKN. The transition points from cw to MI to CS are indicated by Δ_{MI}^f , Δ_{\uparrow}^f , and Δ_{max}^f , respectively.

very useful in retrieving the threshold values of system parameters that initiate the time-stationary pattern structures [38]. Importantly, this study also facilitates insight into the impact of various physical processes on the steady-state solution of the LLE, as pattern structures and cw solutions coexist to form the CS [1]. In the presence of FDKN, the *steady-state* ($\partial u/\partial t = 0$) and *homogeneous* ($\partial u/\partial \tau = 0$) solution of the intracavity field amplitude u_s of Eq. (1) that satisfies the cubic equation is

$$X = \alpha^2 Y^3 - 2\alpha \Delta Y^2 + (\Delta^2 + 1)Y, \quad (2)$$

where $\alpha = \text{sgn}(\gamma_{0\text{eff}}) + [\Gamma - \text{sgn}(\gamma_{0\text{eff}})]f_R$, with $Y = |u_s|^2$ and $X = |S|^2$ being the normalized intracavity field power and driving field power, respectively.

Exploiting the bistability equation [Eq. (2)], we calculate an analytical expression of the steady-state intracavity power Y_{\pm}^f for FDKN by setting $dX/dY = 0$,

$$Y_{\pm}^f = \frac{2\Delta \pm \sqrt{\Delta^2 - 3}}{3\alpha}. \quad (3)$$

Equation (3) reveals the values of threshold detuning $\Delta_c^f = -\sqrt{3}$ for launching ① and $\Delta_c^f = +\sqrt{3}$ for launching ② beyond which bistability emerges, and Eq. (2) yields three solutions for Y for each case. Also from Eqs. (2) and (3), the turning points (X_{\pm}) of the input power on the bistability curve for a fixed Δ can be calculated as

$$X_{\pm}^f = \frac{2}{27\alpha} [\Delta(\Delta^2 + 9) \pm \sqrt{\Delta^2 - 3}^3]. \quad (4)$$

It is also conceivable that Eq. (2) can be interpreted in an alternative yet similar way in terms of Δ as

$$\Delta^f = \alpha Y \pm \sqrt{X/Y - 1}. \quad (5)$$

Note that in the absence of FDKN [$\Gamma = 1$, and $\text{sgn}(\gamma_{0\text{eff}} = \gamma_{0\text{undoped}}) = +1$; i.e., $\alpha = 1$], Eqs. (2)–(5) reduce to the well-known expressions of Kerr optical bistability for the unperturbed LLE [38].

In Figs. 3(a) and 3(b), we plot the steady-state cw response in (Δ, Y) and (X, Y) parameter space for two launching conditions ① and ②, where negative and positive Kerr tilts are evident in Fig. 3(a). Case ① shows that cw bistability occurs only for the negative detuning, suggesting the existence of CS with negative Δ only [shown in Fig. 2(a)]. The cw-bistability S curve is shown in Fig. 3(b) with the turning points X_{\pm}^f that separate the lower and upper stable branches (solid portion) from the unstable intermediate branch (dashed portion) that does not support any stable solution. The interpretation of the unstable branch can be understood from the MI analysis. It is important to note that while $\mu_{1\text{eff}}$ and τ_{sh} do not contribute to the steady-state solution, they have a direct impact on the MI gain. In this context, although δ_3 has no effect on the frequency of MI [52], it does affect the stability of the Kerr frequency combs induced by MI in resonators [53]. Furthermore, it has been well established that IRS has no effect on the homogeneous steady-state solution or the MI gain, but it stabilizes the traveling localized structures [5, 13, 14]. All these perturbations, however, affect the stability of the CS and limit

the dynamics over the parameters set (X, Δ) , which we try to analyze using the variational method.

V. INTRACAVITY MODULATION-INSTABILITY ANALYSIS

In the context of nonlinear optics, MI arises due to the interplay between dispersion and the nonlinear Kerr effect. In this process, a homogeneous field spontaneously breaks up into a periodic structure. In microresonators, the intracavity MI leads to time stationary periodic structures generated from the breaking of a homogeneous wave [39,54]. The MI analysis is performed by introducing the ansatz to Eq. (1) of the form $u(t, \tau) = u_s + a_+(t)e^{i\Omega\tau} + a_-(t)e^{-i\Omega\tau}$, where u_s is the steady-state cw solution of Eq. (1) which follows from the bistability analysis, and a_{\pm} are the two small side-band amplitudes with normalized side-band frequency Ω . This analysis leads to the set of coupled differential equations for a_{\pm} , which upon linearization have the form (excluding the τ_R term)

$$\frac{\partial}{\partial t} \begin{bmatrix} a_+ \\ a_-^* \end{bmatrix} = \begin{bmatrix} a_1 + a_2 & (a_3 + a_4)u_s^2 \\ (a_3 - a_4)u_s^{*2} & a_1 - a_2 \end{bmatrix} \begin{bmatrix} a_+ \\ a_-^* \end{bmatrix} \equiv \mathcal{M} \begin{bmatrix} a_+ \\ a_-^* \end{bmatrix}, \quad (6)$$

where $a_1 = -1 - i2\mathcal{T}_{\text{sh}}\Omega Y - i\delta_3\Omega^3$, $a_2 = i(2\alpha Y - \Delta + \delta_2\Omega^2)$, $a_3 = -i\mathcal{T}_{\text{sh}}\Omega$, and $a_4 = i\alpha$, with $\mathcal{T}_{\text{sh}} = \mu_{\text{1eff}}(1 - f_R) + \Gamma\tau_{\text{sh}}f_R$. This matrix equation contains all the perturbations associated with the system. The intracavity MI gain can be calculated by evaluating the eigenvalues of the matrix equation $|\mathcal{M} - \Lambda I| = 0$, which in this case takes the form

$$\Lambda^f = -1 \pm \sqrt{Y^2(\alpha^2 - \mathcal{T}_{\text{sh}}^2\Omega^2) - \tilde{\delta}_f^2}, \quad (7)$$

where $\tilde{\delta}_f = (2\alpha Y + \delta_2\Omega^2 - \Delta)$. Equation (7) implies that a real positive value of Λ^f leads to instability. In the case of cw perturbations ($\Omega = 0$), this leads to the condition $\sqrt{4\alpha Y\Delta - \Delta^2 - 3\alpha^2 Y^2} \geq 1$, which is simply the negative slope of the bistability S curve (intermediate unstable branch) [Fig. 3(b)]. Therefore, this analysis concludes that the upper and lower branches are always stable against steady-state cw perturbations, while the middle branch is always unstable. This stability condition, however, is modified when a periodic perturbation is present (i.e., $\Omega \neq 0$). For that, we first calculate the threshold conditions of intracavity MI by setting $\Lambda^f = 0$ and analyze the stable and unstable regions in both ① ($\delta_2 = +1$) and ② ($\delta_2 = -1$). In the case of $\mathcal{T}_{\text{sh}} = 0$, the threshold conditions take the form

$$Y \geq 1/|\alpha| \quad \text{and} \quad Y \geq \Delta/(2\alpha). \quad (8)$$

In Figs. 3(c) and 3(e), we plot the bistability S curve in (X, Y) for ① (with $\Delta = -3.5$ and $\alpha = -0.6418$) and for ② (with $\Delta = 3.5$ and $\alpha = 0.9362$), respectively. The modulationally unstable regions (shaded areas) followed by Eq. (8) are plotted in Figs. 3(d) and 3(f) and are mapped with the corresponding (X, Y) plots. This mapping indicates that unlike cw perturbations, periodic perturbations make the upper branch unstable [dashed portion of the S curves in Figs. 3(c) and 3(e)]. From Eq. (5), the minimum detuning that initiates intracavity MI is expressed using the threshold MI conditions as $\Delta_{\text{MI}}^f = \text{sgn}(\alpha)(1 - \sqrt{|\alpha|X - 1})$. Also, in between

the wavelength range of ZNF and ZDF ($\beta_2 > 0$, $\gamma_{\text{eff}} > 0$) in Fig. 1(b) and another region when ZDF is located at the left side of the ZNF ($\beta_2 < 0$, $\gamma_{\text{eff}} < 0$), the threshold conditions of MI become $1/|\alpha| \leq Y \leq \Delta/(2\alpha)$ and $\Delta \geq 2\alpha/|\alpha|$. Note that in self-focusing nonlinearity, the intracavity MI occurs for both the ND and AD regimes with different threshold conditions [1]. Here, in the case of FDKN, due to the reversal of the sign of nonlinearity, we have the same type of threshold conditions, albeit with a different range of parameters. Also, we can calculate the transition detuning from MI to CS (Δ_{\uparrow}^f) from Eq. (5) by setting $d\Delta/dY = 0$ and substituting the Y values back into Eq. (5), which is the same procedure as getting Eq. (4) from Eq. (2). In Fig. 3(g), we plot the MI gain spectrum [$\Lambda^f(\Omega)$] at $Y = 3.5$ for both ① and ②. The MI gain spectrum is both dispersion and nonlinearity dependent owing to the FDKN. As a result, the phase mismatch can be canceled in both AD and ND domains, which leads to the MI gain at low threshold power. Now, in the presence of perturbations, the maximum MI gain occurs ($d\Lambda^f/d\Omega = 0$) when Ω satisfies the relation $\delta_2\Omega_{\text{max}}^2 = \Delta - 2\alpha Y - \mathcal{T}_{\text{sh}}^2 Y^2/(2\delta_2)$. In this case, Ω is real as long as $\mathcal{T}_{\text{sh}}^2 \leq 2\delta_2(\Delta - 2\alpha Y)/Y^2$. This analytical expression provides a cutoff value for the strength of \mathcal{T}_{sh} required for MI to occur or, in other words, it gives a threshold range of Δ to observe MI for a fixed \mathcal{T}_{sh} . Also, the maximum gain can be calculated as $\Lambda_{\text{max}}^f = -1 + \sqrt{\alpha^2 Y^2 - \mathcal{T}_{\text{sh}}^2 Y^2 \Omega_{\text{max}}^2}$. This Λ_{max}^f indicates that in both the launching conditions ① and ②, the nature of the MI gain curves is similar, as seen from Fig. 3(g). From the expression of Λ_{max}^f , one can calculate the condition of the steady-state solution that is always stable for $Y \leq 1/\sqrt{\alpha^2 - \mathcal{T}_{\text{sh}}^2 \Omega_{\text{max}}^2}$, which provides the minimum intracavity intensity to initiate the MI. In order to get complete dynamics, in Fig. 3(h) we plot intracavity cw solutions (black curve), the peak intensities of MI patterns (blue dashed line), and the CS branch (solid blue line) as a function of Δ . In this case, our calculated value of $Y_{\text{min}} = 1.57$ matches with the numerical value of $Y \approx 1.6$ to trigger the MI. We also indicate the transition detuning point of MI from cw solutions, $\Delta_{\text{MI}}^f = 0.374$ (numerically: $\Delta \approx 0.37$), the onset detuning $\Delta_{\uparrow}^f = -2.373$ (numerically: $\Delta \approx -2.387$), and the numerical value of maximum detuning $\Delta_{\text{max}}^f = -3.029$ of the CS branch [38]. In the next section, the analytical expression of Δ_{max}^f is calculated using the variational method.

VI. PERTURBATIVE ANALYSIS: VARIATIONAL METHOD

The LLE describing the nanoparticle composite microresonator with FDKN includes all the perturbations, i.e., linear loss, ZNF, self-steepening, and IRS, and the effects are investigated numerically by directly solving Eq. (1). However, this numerical solution does not provide detailed information about exactly how these perturbations affect the CS parameters. To get deeper insights into these perturbations, we adopt a semianalytic variational method. Even though the concept of the variational principle is generally known in classical mechanics, the use of the method has been extended in the context of pulse propagation problems in nonlinear media with excellent success [32,47,55]. In this work, for variational analysis, we consider Eq. (1) as a perturbed field equation

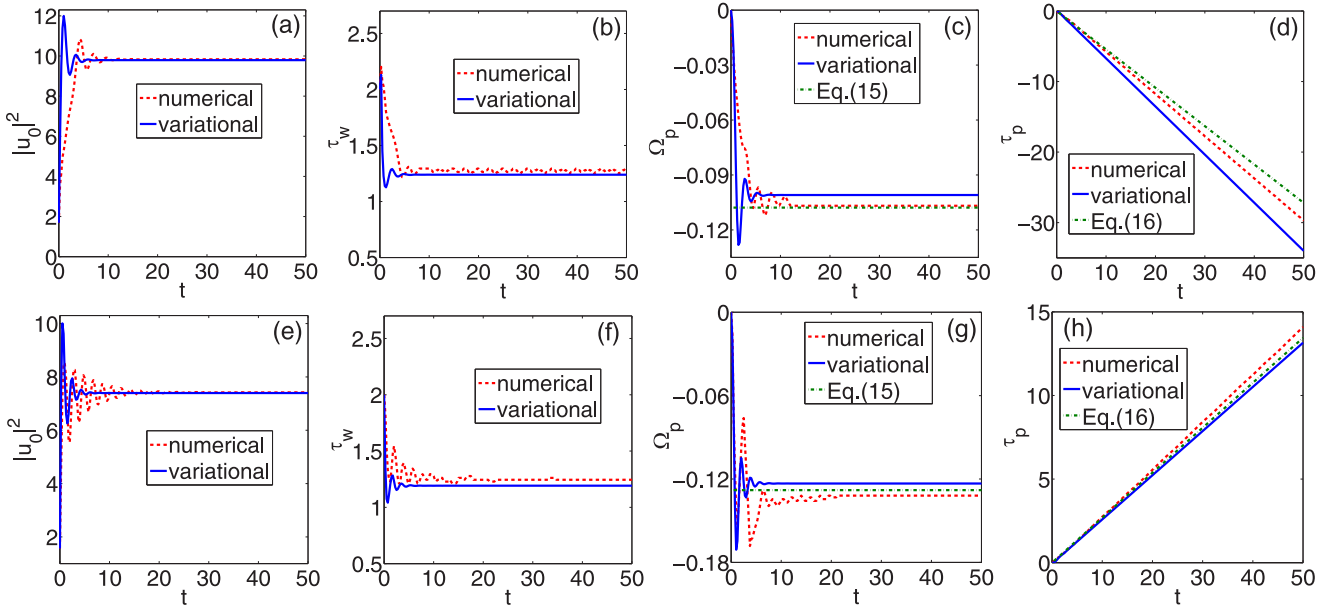


FIG. 4. The variation of (a) peak intensity ($|u_0|^2$), (b) temporal pulse width ($\tau_w = 2\eta^{-1}$), (c) frequency shift (Ω_p), and (d) temporal delay (τ_p) of a CS over the round-trip time t for $\textcircled{1}$. Similarly, (e)–(h) represent the same for $\textcircled{2}$. The closed form of the saturated frequency [Eq. (15)] and corresponding temporal shift [Eq. (16)] are also plotted by dot-dashed lines.

as $i\frac{\partial u}{\partial t} - \delta_2 \frac{\partial^2 u}{\partial \tau^2} + a|u|^2 u - \Delta u = i\epsilon(u)$, where $\epsilon(u)$ contains all the first-order perturbations of the system: $\epsilon(u) = S - u - i(a - \Gamma)f_R|u|^2 u - \mathcal{T}_{\text{sh}}\frac{\partial(|u|^2 u)}{\partial \tau} - i\mathcal{T}_{\mathcal{R}}u\frac{\partial|u|^2}{\partial \tau}$. We define the Lagrangian density ($\mathcal{L}_{\mathcal{D}}$) for such a system as $\mathcal{L}_{\mathcal{D}} = \frac{i}{2}(u^* \frac{\partial u}{\partial t} - u \frac{\partial u^*}{\partial t}) + \delta_2 |\frac{\partial u}{\partial \tau}|^2 + \frac{a}{2}|u|^4 - \Delta|u|^2 - 2\text{Re}[i\epsilon u^*]$. The given Lagrangian density is reduced as $L(= \int_{-\infty}^{\infty} \mathcal{L}_{\mathcal{D}} d\tau)$ through the general ansatz:

$$u(t, \tau) = \left[\frac{E(t)\eta(t)}{2} \right]^{1/2} \text{sech}\{\eta(t)[\tau - \tau_p(t)]\} \times \exp\{i\phi(t) - i\Omega_p(t)[\tau - \tau_p(t)]\}, \quad (9)$$

where the pulse energy (E), inverse of temporal pulse width (η), temporal delay (τ_p), phase (ϕ), and frequency shift (Ω_p) are functions of round-trip time t . The Ritz's optimization procedure for L gives $\frac{d}{dt} \left[\frac{\partial L}{\partial Q} \right] - \frac{\partial L}{\partial Q} = 0$, where the general parameter Q corresponds to the different pulse parameters. Hence, eventually we obtain a set of five coupled equations describing the evolution equation of individual pulse parameters as

$$\frac{dE}{dt} = -2E + 2S \left(\frac{E}{2\eta} \right)^{1/2} \pi \text{sech}(\mathcal{K}/2) \cos \phi, \quad (10)$$

$$\frac{d\tau_p}{dt} = 2\delta_2 \Omega_p + \frac{1}{2} \mathcal{T}_{\text{sh}} E \eta, \quad (11)$$

$$\frac{d\Omega_p}{dt} = -\frac{4}{15} \mathcal{T}_{\mathcal{R}} E \eta^3 - 2S \left(\frac{\eta}{2E} \right)^{1/2} \mathcal{K} \text{sech}(\mathcal{K}/2) \cos \phi, \quad (12)$$

$$\frac{d\phi}{dt} = -\Delta - \delta_2 \left(\Omega_p^2 - \frac{\eta^2}{3} \right) + \frac{1}{3} \alpha \eta E - \frac{1}{6} \mathcal{T}_{\text{sh}} E \eta \Omega_p - S \left(\frac{1}{2E\eta} \right)^{1/2} \pi \text{sech}(\mathcal{K}/2) \sin \phi, \quad (13)$$

$$\eta = -\frac{E}{4\delta_2} (\alpha + \mathcal{T}_{\text{sh}} \Omega_p) - \frac{3}{2\delta_2 \eta} S \left(\frac{1}{2E\eta} \right)^{1/2} \times \pi \text{sech}(\mathcal{K}/2) [1 - \mathcal{K} \tanh(\mathcal{K}/2)] \sin \phi, \quad (14)$$

where $\mathcal{K} = \pi \Omega_p / \eta$. The set of equations is important in understanding the dynamics of a CS under FDKN, which facilitates exactly how $\mathcal{T}_{\mathcal{R}}$, μ_{eff} , and τ_{sh} affect different pulse parameters. For instance, $\mathcal{T}_{\mathcal{R}}$ appears in the frequency equation with a negative sign, resulting in a spectral redshift irrespective of the launching condition. The contributions from the FDKN (\mathcal{T}_{sh}) directly appear in the equations for τ_p , ϕ , and η . The presence of the δ_2 factor in the equation for τ_p immediately reveals that even though Ω_p is negative, the temporal CS either accelerates or decelerates depending on the launching condition. However, to get the complete evolution picture of individual pulse parameters, we solve these coupled equations [Eqs. (10)–(14)] semianalytically, and the results are shown by the solid lines in Fig. 4. Next, in order to validate the variational results, we plot the pulse parameters from the direct numerical simulation of Eq. (1). In Figs. 4(a), 4(e) and 4(b), 4(f), we plot $|u_0|^2$ and τ_w over the round-trip time t by dashed lines excluding the cw background because of the fact that the ansatz [Eq. (9)] does not comprise any background field. In both cases, the variational method accurately predicts the numerical results. The frequency shift Ω_p and temporal delay τ_p are plotted in Figs. 4(c), 4(g) and 4(d), 4(h), both numerically (dashed lines) and variationally (solid lines), where a slight deviation is observed at a longer t . This mismatch appears because of our variational ansatz that does not include the frequency chirp parameter. The chirp parameter makes the $\mathcal{L}_{\mathcal{D}}$ nonintegrable, and we cannot get any closed-form expressions out of it. Note that unlike the conventional Kerr soliton, here the pulse parameters ($|u_0|^2$, τ_w , and Ω_p) oscillate at the very beginning of the evolution and saturate

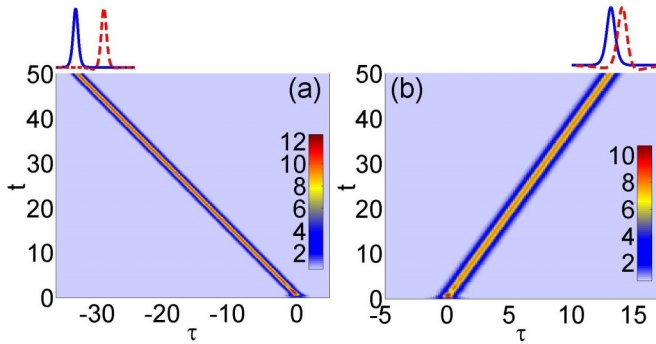


FIG. 5. Temporal evolution of the variational ansatz [Eq. (9)] for (a) ① and (b) ② under the influence of perturbations, whose pulse parameters are governed by Eqs. (10)–(14). The output pulse shapes from the variational ansatz (solid blue curve) and the numerical CS profile (red dotted curve) are shown on the top of each panel.

to steady values over the t . The variational method also captures this initial oscillation, where the phase (ϕ) stabilizes the ansatz parameters via $\sin \phi$ and $\cos \phi$ terms associated with the evolution equations. The steady-state saturated frequency can be obtained from Eq. (12) by setting $d\Omega_p^{\text{sat}}/dt = 0$ and assuming $\text{sech}(\mathcal{K}_{\text{sat}}/2) \cos \phi \approx 1$, which takes the form

$$\Omega_p^{\text{sat}} \approx -\frac{4}{15} \left| \frac{\alpha}{\delta_2} \right| \frac{\mathcal{T}_R}{\pi S} u_{0\text{sat}}^5. \quad (15)$$

This saturated frequency (Ω_p^{sat}) leads to a linear temporal shift, which is obtained by integrating (11) as

$$\tau_p(t) \approx (2\delta_2 \Omega_p^{\text{sat}} + \mathcal{T}_{sh} u_{0\text{sat}}^2) t. \quad (16)$$

In Figs. 4(c), 4(g) and 4(d), 4(h), we plot the approximate analytical expressions of Ω_p^{sat} and $\tau_p(t)$ (dot-dashed lines) that closely match both the numerical and full variational results.

The set of coupled equations is further analyzed to obtain the analytical expression of the maximum detuning (in magnitude) for the existence of CSs under FDKN. From Eqs. (10), (13), and (14), the detuning can be derived as [1] $\Delta_{\text{max}}^f = \pi^2 \alpha X / 8$. For a given $X = 4.5$ and at the launching condition ①, the theoretical value is $\Delta_{\text{max}}^f = -3.563$. Numerically, the value appears to be $\Delta \approx -3.029$, which is less than the maximum theoretical limit, suggesting that the higher-order perturbations reduce the range of parameters [50].

For a final check of the accuracy of the variational method in the case of LLE, the trial ansatz [Eq. (9)], and the derived set of coupled equations for pulse parameters [Eqs. (10)–(14)], we plot the temporal evolutions in Figs. 5(a) and 5(b) under perturbations. These figures show similar pulse dynamics as obtained from the direct numerical solution of Eq. (1) [Figs. 2(a) and 2(c)] excluding the HOD terms. As previously mentioned, a slight difference in temporal position between the sech ansatz and the CS is observed at the output because the actual shape of the CS differs slightly from the ansatz. However, as illustrated in Fig. 4, our variational method accurately predicts the overall evolution dynamics and other critical parameters.

VII. IMPACT OF THE ZERO-NONLINEARITY FREQUENCY ON DISPERSIVE WAVES

In optical pulse propagation, while the interplay between the GVD and nonlinearity stabilizes the formation of solitonlike structures in both time and frequency, HOD leads to significant temporal and spectral distortion. Third-order dispersion (TOD) is the first significant term to the HOD that perturbs the soliton to emit dispersive radiation or DW by transferring energy across a ZDF [56]. Such radiation in the form of a plane wave is also known as the nonsolitic or Cherenkov radiation [57]. In the case of a microresonator with a circulating CS pumped at near-zero-dispersion wavelength, the DW formation results in the generation of broadband frequency combs [58]. Here, the DW manifests as a stationary localized oscillatory radiation tail attached to the temporal CS [59]. Also, the IRS-induced self-frequency shift along with the DW in a high-Q resonator plays an essential role in comb dynamics, where the existence of frequency-locked solitons is governed by the balance between Raman gain and cavity loss [60]. In this context, the interplay of the broadband Raman gain and HOD influence the existence and dynamics of the CS. Here, we focus on the interplay between the HOD and frequency-dependent nonlinearity to capture how the ZNF influences dispersive radiation. Also, we try to capture the efficient control of the radiation frequency of the DW through the manipulation of ZNF. In a microresonator with FDKN, a generalized PM equation gives information about the spectral location of the DW in the presence of ZDF and the interaction of it with ZNF. In dimensionless form, the generalized PM equation is written as [58,59,61]

$$\delta_2 \Omega^2 + \delta_3 \Omega^3 - V \Omega + 2(a + \mu_{1\text{eff}} \Omega) - \Delta + i = 0. \quad (17)$$

Here, the group-velocity mismatch (β_v) between the CS and the driving field is rescaled as $V = \sqrt{2\alpha}/(|\beta_2|L)\beta_v/\alpha$, which can be calculated from the slope of the temporal shift of the CS as $V = d\tau_p/dt$. Equation (17) is different from the standard PM equation in the conservative soliton case [47], as it includes additional terms related to microresonator properties, i.e., Δ , 1 (rescaled loss) with imaginary i , and V , as well as the sign and first-order slope of frequency-dependent nonlinear terms, i.e., $a = \text{sgn}(\gamma_{0\text{eff}})$ and $\mu_{1\text{eff}}$. The PM equation [Eq. (17)] contains both real and imaginary (due to dissipative terms) parts and may lead to complex frequencies. The real solution of Eq. (17) gives the detuning frequency of radiation Ω_{DW} , which is the spectral location of the DW. The imaginary part can be interpreted as the decaying tail of the temporal DW structure [59]. In our case, the presence of the ZNF term influences the generated DW and modifies the spectral location. In Figs. 6(a) and 6(b), we plot the spectral evolution of CSs in two operational domains under the influence of strong TOD perturbation ($\delta_3 = 0.2$) with all other parameters the same as Fig. 2. The generation of the DW across a ZDF is evident as a distinct spectral peak. In the same figure, we plot the PM curve [Eq. (17)] as a function of frequency, the zero-crossing point (solid circle) of which represents the Ω_{DW} . In Fig. 6(c), we plot Ω_{DW} as a function of $\mu_{1\text{eff}}$ (i.e., by varying ZNF) both numerically as well as by solving the PM equation. For further verification of the accuracy of our derived PM equation, we plot the variation of Ω_{DW} as a function of δ_3 for fixed $\mu_{1\text{eff}}$ in

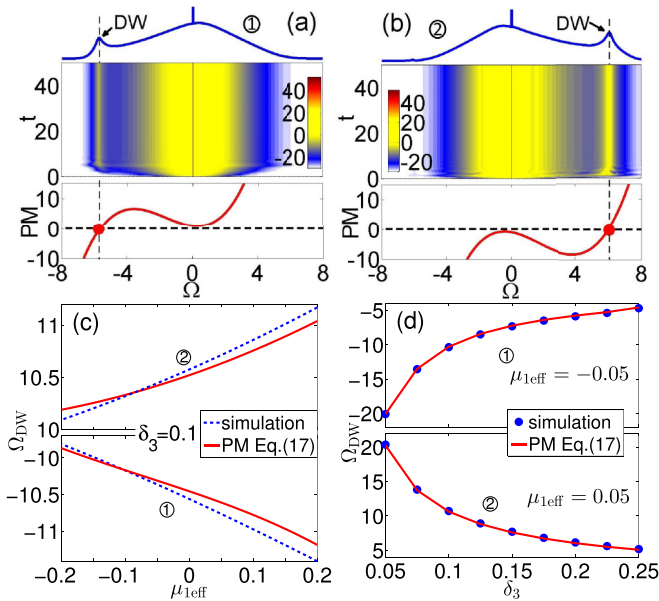


FIG. 6. (a),(b) Spectral evolution of CSs under the influence of a strong TOD ($\delta_3 = 0.2$) for two launching conditions. The upper panel corresponds to the output spectrum. The lower panel in each plot represents the graphical solution of the PM equation [Eq. (17)] with zero-crossing frequency that gives the location of the DW. Variation of the radiation frequency with (c) μ_{eff} and (d) δ_3 for two launching conditions. All the other parameters are the same as in Fig. 2.

Fig. 6(d). The PM equation (solid curves) accurately predicts the numerical simulation data (solid circles). It is clear from these plots that the ZNF appears to have a substantial role in influencing the dynamics of the DW, and the location of the DW is altered as a result of the interaction between the ZDF and ZNF. So, we have two independent parameters that can efficiently tune the spectral location of the DW. Furthermore, unlike conventional fibers, where the GVD profile and the ZDF can only be varied by changing the cross-sectional geometry or the materials, the ZNF of doped fiber can be easily changed by changing the doping concentration.

VIII. CONCLUSIONS

In this paper, we study the dynamics of cavity solitons under frequency-dependent Kerr nonlinearity in a silica resonator whose core is doped with silver nanoparticles. For such a resonator, the modified mean-field Lugiato-Lefever equation contains higher-order nonlinear effects (intrapulse Raman scattering, self-steepening, and zero-nonlinearity frequency) that act as perturbations and influence the intracavity field dynamics. Depending on the launching conditions and controlling system parameters, it is possible to excite bright cavity solitons in both solitonic domains. Exploiting the steady-state continuous-wave bistability analysis and intracavity modulation-instability analysis, we derive modified analytical expressions of different stability regions and critical values of system parameters for the existence of cavity solitons under frequency-dependent Kerr nonlinearity. Further, we develop a variational technique to capture the cavity-soliton dynamics analytically. The phenomena of a cavity-soliton-mediated dispersive wave and how the spectral location of it can be manipulated through the interplay between the zero-dispersion frequency and zero-nonlinearity frequency are captured by providing a modified phase matching equation. Our analysis provides a framework for a better understanding of the insights into self-organized states of light. We envisage that our results and methodology are applicable in different microresonator-based frequency comb studies, such as two-soliton interaction [7], dual-pump spectroscopy [62], formation of frequency molecules [63], spectral extension of frequency combs [64], and manipulation of counterpropagating solitons [65] in two-solitonic domains.

ACKNOWLEDGMENTS

A.S. acknowledges the Ministry of Human Resource Development (MHRD), India for a research fellowship through IPDF IIT Guwahati. A.K.S. acknowledges support from the Science and Engineering Research Board (SERB), under the project MATRICS (Grant No. MTR/2019/000945).

- [1] P. Grelu, *Nonlinear Optical Cavity Dynamics: From Microresonators to Fiber Lasers* (Wiley, New York, 2016).
- [2] T. J. Kippenberg, R. Holzwarth, and S. A. Diddams, *Science* **332**, 555 (2011).
- [3] A. Pasquazi *et al.*, *Phys. Rep.* **729**, 1 (2018).
- [4] L. A. Lugiato and R. Lefever, *Phys. Rev. Lett.* **58**, 2209 (1987).
- [5] A. J. Scroggie, W. J. Firth, G.S. McDonald, M.Tlidi, R. Lefever, and L. A. Lugiato, *Chaos Solitons Fract.* **4**, 1323 (1994).
- [6] M. Tlidi, P. Mandel, and R. Lefever, *Phys. Rev. Lett.* **73**, 640 (1994).
- [7] K. Krupa, K. Nithyanandan, U. Andral, P. Tchofo-Dinda, and P. Grelu, *Phys. Rev. Lett.* **118**, 243901 (2017).
- [8] H. Bao *et al.*, *Nat. Photon.* **13**, 384 (2019).
- [9] L. Del Bino, J. M. Silver, S. L. Stebbings, and P. Del'Haye, *Sci. Rep.* **7**, 43142 (2017).
- [10] R. El-Ganainy, K. G. Makris, M. Khajavikhan, Z. H. Musslimani, S. Rotter, and D. N. Christodoulides, *Nat. Phys.* **14**, 11 (2018).
- [11] H. Taheri and A. B. Matsko, *Opt. Lett.* **44**, 3086 (2019).
- [12] H. Wang, Y.K. Lu, L. Wu, D. Y. Oh, B. Shen, S. H. Lee, and K. Vahala, *Light Sci. Appl.* **9**, 205 (2020).
- [13] M. G. Clerc, S. Coulibaly, and M. Tlidi, *Phys. Rev. Research* **2**, 013024 (2020).
- [14] M. G. Clerc, S. Coulibaly, P. Parra-Rivas, and M. Tlidi, *Chaos* **30**, 083111 (2020).
- [15] P. Parra-Rivas, S. Coulibaly, M. G. Clerc, and M. Tlidi, *Phys. Rev. A* **103**, 013507 (2021).
- [16] F. Leo, L. Gelens, P. Emplit, M. Haelterman, and S. Coen, *Opt. Express* **21**, 9180 (2013).
- [17] P. Parra-Rivas, D. Gomila, L. Gelens, and E. Knobloch, *Phys. Rev. E* **97**, 042204 (2018).

- [18] C. Godey, I. V. Balakireva, A. Coillet, and Y. K. Chembo, *Phys. Rev. A* **89**, 063814 (2014).
- [19] Y. Xu, A. Sharples, J. Fatome, S. Coen, M. Erkintalo, and S. G. Murdoch, *Opt. Lett.* **46**, 512 (2021).
- [20] R. W. Boyd, S. G. Lukishova, and Y. R. Shen, *Self-focusing: Past and Present* (Springer-Verlag, New York, 2009).
- [21] R. Driben and J. Herrmann, *Opt. Lett.* **35**, 2529 (2010).
- [22] V. Smith, B. Leung, P. Cala, Z. Chen, and W. Man, *Opt. Mater. Express* **4**, 1807 (2014).
- [23] G. Liang, W. Hong, T. Luo, J. Wang, Y. Li, Q. Guo, W. Hu, and D. N. Christodoulides, *Phys. Rev. A* **99**, 063808 (2019).
- [24] R. Driben, A. Husakou, and J. Herrmann, *Opt. Express* **17**, 17989 (2009).
- [25] S. Bose, A. Sahoo, R. Chattopadhyay, S. Roy, S. K. Bhadra, and G. P. Agrawal, *Phys. Rev. A* **94**, 043835 (2016).
- [26] A. Sahoo and S. Roy, *J. Opt. Soc. Am. B* **36**, 2352 (2019).
- [27] G. P. Agrawal, *Phys. Rev. Lett.* **64**, 2487 (1990).
- [28] L. J. Qian, X. Liu, and F. W. Wise, *Opt. Lett.* **24**, 166 (1999).
- [29] I. Towers and B. A. Malomed, *J. Opt. Soc. Am. B* **19**, 537 (2002).
- [30] D. Turchinovich, J. M. Hvam, and M. C. Hoffmann, *Phys. Rev. B* **85**, 201304(R) (2012).
- [31] S. Bose, R. Chattopadhyay, S. Roy, and S. K. Bhadra, *J. Opt. Soc. Am. B* **33**, 1014 (2016).
- [32] D. Anderson, *Phys. Rev. A* **27**, 3135 (1983).
- [33] S. Wabnitz, *Opt. Lett.* **18**, 601 (1993)
- [34] D. J. Kaup and B. M. Malomed, *Physica D* **87**, 155 (1995).
- [35] W. B. Cardoso, L. Salasnich, and B. A. Malomed, *Sci. Rep.* **7**, 16876 (2017).
- [36] A. Sahoo and S. Roy, *Phys. Rev. A* **100**, 053814 (2019).
- [37] H. M. Gibbs, *Optical Bistability: Controlling Light with Light* (Academic, New York, 1985).
- [38] S. Coen and M. Erkintalo, *Opt. Lett.* **38**, 1790 (2013).
- [39] T. Hansson, D. Modotto, and S. Wabnitz, *Phys. Rev. A* **88**, 023819 (2013).
- [40] The single-mode fiber consists of a silica cladding and 6.3% GeO₂-doped silica core. Coefficients of the Sellmeier's formula are adopted from A. Ghatak and K. Thyagarajan, *An Introduction to Fiber Optics* (Cambridge University Press, Cambridge, 1998).
- [41] S. Bose, R. Chattopadhyay, and S. K. Bhadra, *Opt. Commun.* **412**, 226 (2018).
- [42] J. C. M. Garnett, *Philos. Trans. R. Soc. London* **203**, 385 (1904).
- [43] J. E. Sipe and R. W. Boyd, *Phys. Rev. A* **46**, 1614 (1992).
- [44] D. D. Smith, G. Fischer, R. W. Boyd, and D. A. Gregory, *J. Opt. Soc. Am. B* **14**, 1625 (1997).
- [45] E. L. Falcão-Filho, C. B. de Araújo, A. Galembeck, M. M. Oliveira, and A. J. G. Zarbin, *J. Opt. Soc. Am. B* **22**, 2444 (2005).
- [46] F. R. Arteaga-Sierra, A. Antikainen, and G. P. Agrawal, *Phys. Rev. A* **98**, 013830 (2018).
- [47] G. P. Agrawal, *Nonlinear Fiber Optics*, 5th ed. (Academic, New York, 2013).
- [48] J. Bonetti, N. Linale, A. D. Sánchez, S. M. Hernandez, P. I. Fierens, and D. F. Grosz, *J. Opt. Soc. Am. B* **37**, 445 (2020).
- [49] N. Linale, P. I. Fierens, and D. F. Grosz, *IEEE J. Quantum Electron.* **57**, 1 (2021).
- [50] Y. Wang, M. Anderson, S. Coen, S. G. Murdoch, and M. Erkintalo, *Phys. Rev. Lett.* **120**, 053902 (2018).
- [51] J. Hult, *J. Lightwave Technol.* **25**, 3770 (2007)
- [52] L. Bahloul, L. Cherbi, A. Hariz, and M. Tlidi, *Philos. Trans. R. Soc. A* **372**, 20140020 (2014).
- [53] P. Parra-Rivas, D. Gomila, F. Leo, S. Coen, and L. Gelens, *Opt. Lett.* **39**, 2971 (2014).
- [54] M. Haelterman, S. Trillo, and S. Wabnitz, *Opt. Lett.* **17**, 745 (1992).
- [55] A. Sahoo, S. Roy, and G. P. Agrawal, *Phys. Rev. A* **96**, 013838 (2017).
- [56] D. V. Skryabin and A. V. Gorbach, *Rev. Mod. Phys.* **82**, 1287 (2010).
- [57] N. Akhmediev and M. Karlsson, *Phys. Rev. A* **51**, 2602 (1995).
- [58] H. Guo, C. Herkommer, A. Billat *et al.*, *Nat. Photon.* **12**, 330 (2018).
- [59] J. K. Jang, M. Erkintalo, S. G. Murdoch, and S. Coen, *Opt. Lett.* **39**, 5503 (2014).
- [60] C. Milián, A. V. Gorbach, M. Taki, A. V. Yulin, and D. V. Skryabin, *Phys. Rev. A* **92**, 033851 (2015).
- [61] C. Milián and D. V. Skryabin, *Opt. Express* **22**, 3732 (2014).
- [62] T. Hansson and S. Wabnitz, *Phys. Rev. A* **90**, 013811 (2014).
- [63] O. Melchert, S. Willms, S. Bose, A. Yulin, B. Roth, F. Mitschke, U. Morgner, I. Babushkin, and A. Demircan, *Phys. Rev. Lett.* **123**, 243905 (2019).
- [64] S. Zhang, J. M. Silver, T. Bi, and P. Del'Haye, *Nat. Commun.* **11**, 6384 (2020).
- [65] Q.-F. Yang, X. Yi, and K. Vahala, *Nat. Photon.* **11**, 560 (2017).